Laminar Tube Flow through an Abrupt Contraction

E. B. CHRISTIANSEN, S. J. KELSEY, and T. R. CARTER

Department of Chemical Engineering
University of Utah, Salt Lake City, Utah

The general equations of motion were solved numerically for the laminar isothermal flow of Newtonian fluids from a large tube of circular cross section through an abrupt contraction into a coaxial tube of smaller diameter and through the flow-development region of the smaller tube. The ratio of the diameter of the large tube to that of the smaller tube was varied from one to eight (the latter in one case). Solutions were obtained for the case where the larger tube is real, with no slip at the wall, and for the case where it is a frictionless "stream" tube. The results are presented as charts giving excess pressure losses attributable to contracted and developing flow in terms of equivalent smaller-tube diameters as functions of the tube-contraction ratio and the Reynolds number, which was varied from 0.01 to as high as 500 in one case. Both radial- and axial-velocity profiles are presented. The computed results are shown to be in satisfactory agreement with some experimental data. The results are presented in a manner convenient for use in the design of equipment in which contracted Newtonian flow occurs, such as fiber spinnerettes and heat exchangers, and in the analysis of experimental data for contracted flow.

The flow of a fluid from a reservoir up to and through the entrance region of a tube of circular cross section is encountered in many situations, such as in fiber spinning, tubular heat exchangers, and capillary-tube viscometry.

In this paper the results of numerical solutions of the equations of motion for the isothermal flow of Newtonian fluids through a sudden contraction are presented. Two flow models are used in the numerical solutions. The larger upstream tube is a stream tube, impermeable and frictionless, and the smaller downstream tube is a real tube, with no slip at the tube wall—the stream-tube/real-tube (ST-RT) model. Both the upstream and downstream tubes are real—the real-tube/real-tube (RT/RT) case. In both cases, the upstream tube is connected to the real tube downstream by a real-surface contraction perpendicular to the tube axis. These flow models are generalizations of the flow model used by Vrentas, Duda, and Bargeron (*15*) for flow in circular tubes of constant cross section.

MATHEMATICAL PROCEDURES

The solution spaces or models are bounded in the radial r direction by cylindrical surfaces which form the tube walls and are unbounded in the axial z direction. That portion of the solution space enclosing the negative part of the z axis is the upstream tube. The contraction is at $z = 0$. The advantage in using the unbounded solution space is that the boundary conditions at $z = \pm\infty$ may be specified as the limiting case of flow in each section, too far removed from the contraction to be influenced by conditions there. Since an unbounded region presents difficulty in numerical computations, a transformation (*15*)

$$\xi = \tanh(kz) \qquad (1)$$

is used, which maps the r-z plane into the r-ξ plane such that the solution space is bounded by $\xi = \pm 1$. The condition of axial symmetry makes it possible to discretize the r-ξ solution space as a rectangular grid, including both the upstream tube $0 \leq r \leq R_u$, $-1 \leq \xi < 0$ and the downstream tube $0 \leq r \leq R_d$, $0 \leq \xi \leq +1$. In most of the computations, the solution space was discretized into ten radial and ten axial divisions in the small tube and 10β [see Equation (2)] radial and ten axial divisions in the larger, or upstream, tube. This will be referred to as a 10 × 20 grid. Many 20 × 20 and some 30 and 40 × 20 and 10 × 30 and 40 grids were also used for improved accuracy and to test convergence.

Summarized in this paper are the results of three solutions of the equations of motion:

1. In the case of ST-RT flow, for which

$$\beta = \frac{\text{Diameter of upstream (larger) tube}}{\text{Diameter of downstream tube}} = 1.0 \qquad (2)$$

vorticity-transport equations similar to those used by Vrentas et al (*15*) were solved by a numerical procedure using relaxation (VT-R method) (*5*).

2. The vorticity-transport equations were solved also for ST-RT and RT-RT flow for $\beta = 1$ to as high as 8 by quasilinearization and the method of lines (QL-ML method) (*9*). This procedure appeared to improve accuracy for the same computational time at the higher N_{Re} as compared with the other methods.

3. The fourth-order stream-function equations were solved by relaxation (SF-R method) for $\beta = 1$ to 4. These computations seemed to be more stable than were those for the solution of the vorticity-transport equations by relaxation (*5*).

The QL-ML method does not require replacement of the no-slip (Cauchy) condition at the wall with the corresponding values of the vorticity. This simplifies the accommodation of the singularity at the tube-entrance corner. In this case, the necessary derivatives of the stream

---

T. R. Carter is now with TRW, Inc., Redondo Beach, California. S. J. Kelsey is with Computer Science Division, University of Utah.

function and vorticity at the corner were obtained using an average of the backward-difference formulae from the four directions.

The procedure in which the fourth-order stream-function equations were used will now be described in some detail. For the steady state, axisymmetrical, isothermal flow of a Newtonian fluid of constant density, the dimensionless forms of the axial and radial components of the equation of motion in cylindrical coordinates are

z Component

$$V\frac{\partial U}{\partial r} + U\frac{\partial U}{\partial z} = -\frac{1}{\rho U_0^2}\frac{\partial P}{\partial z} + \frac{1}{N_{Re}}\left[\frac{1}{r}\frac{\partial}{\partial r}\left[r\frac{\partial U}{\partial r}\right] + \frac{\partial^2 U}{\partial z^2}\right] \quad (3)$$

r Component

$$V\frac{\partial V}{\partial r} + U\frac{\partial V}{\partial z} = -\frac{1}{\rho U_0^2}\frac{\partial P}{\partial r} + \frac{1}{N_{Re}}\left[\frac{\partial}{\partial r}\left[\frac{1}{r}\frac{\partial (rV)}{\partial r}\right] + \frac{\partial^2 V}{\partial z^2}\right] \quad (4)$$

where all velocities have been referred to the average velocity in the downstream tube U_0 and the length dimensions have been referred to the diameter of the downstream tube D. In this coordinate system, the equation of continuity is

$$\frac{1}{r}\rho\frac{\partial (rV)}{\partial r} + \rho\frac{\partial U}{\partial z} = 0 \quad (5)$$

If Equation (4) is differentiated with respect to z, Equation (3) differentiated with respect to r, and the difference of the two equations formed, there results one equation involving V and U. The terms involving the pressure gradients $\partial P/\partial r$ and $\partial P/\partial z$ cancel, assuming that the pressure function is of the required degree of continuity to insure equality of the cross partials formed in the above differentiations. Finally, by substitution of the stream-function-velocity relationship

$$V = \frac{1}{r}\frac{\partial\psi}{\partial z}, \quad U = -\frac{1}{r}\frac{\partial\psi}{\partial r} \quad (6)$$

the following equation is formed

$$\begin{aligned}\frac{1}{N_{Re}}&\left[\frac{\partial^4\psi}{\partial r^4} + 2\frac{\partial^4\psi}{\partial r^2\,\partial z^2} + \frac{\partial^4\psi}{\partial z^4}\right] - \left[\frac{1}{r}\frac{\partial\psi}{\partial z} + \frac{2}{r\,N_{Re}}\right]\frac{\partial^3\psi}{\partial r^3} \\ &- \left[\frac{1}{r}\frac{\partial\psi}{\partial z} + \frac{2}{r\,N_{Re}}\right]\frac{\partial^3\psi}{\partial r\,\partial z^2} + \left[\frac{1}{r}\frac{\partial\psi}{\partial r}\right]\frac{\partial^3\psi}{\partial r^2\,\partial z} + \left[\frac{1}{r}\frac{\partial\psi}{\partial r}\right]\frac{\partial^3\psi}{\partial z^3} \\ &+ \left[\frac{3}{r^2}\frac{\partial\psi}{\partial z} + \frac{3}{r^2\,N_{Re}}\right]\frac{\partial^2\psi}{\partial r^2} - \left[\frac{1}{r^2}\frac{\partial\psi}{\partial r}\right]\frac{\partial^2\psi}{\partial r\,\partial z} \\ &+ \left[\frac{2}{r^2}\frac{\partial\psi}{\partial z}\right]\frac{\partial^2\psi}{\partial z^2} - \left[\frac{3}{r^3}\frac{\partial\psi}{\partial z} + \frac{3}{r^3\,N_{Re}}\right]\frac{\partial\psi}{\partial r} = 0 \quad (7)\end{aligned}$$

By repeated application of the chain rule for derivatives

$$\frac{\partial\psi}{\partial z} = \frac{\partial\psi}{\partial\xi}\frac{d\xi}{dz}$$

Equation (7) may be converted to the form

$$\begin{aligned}\frac{1}{N_{Re}}&\left[\frac{\partial^4\psi}{\partial r^4} + 2\frac{\partial^4\psi}{\partial r^2\,\partial\xi^2} + \frac{\partial^4\psi}{\partial\xi^4}\right] + A\frac{\partial^3\psi}{\partial r^3} \\ &+ B\frac{\partial^3\psi}{\partial r^2\,\partial\xi} + C\frac{\partial^3\psi}{\partial r\,\partial\xi^2} + D\frac{\partial^3\psi}{\partial\xi^3} + E\frac{\partial^2\psi}{\partial r^2} \\ &+ F\frac{\partial^2\psi}{\partial r\,\partial\xi} + G\frac{\partial^2\psi}{\partial\xi^2} + H\frac{\partial\psi}{\partial r} = 0 \quad (8)\end{aligned}$$

which is suitable for use in the r-ξ space obtained from the r-z space by the transformation Equation (1). In the computations, the constants A to H are evaluated using previous values of the stream function.

For the region composed of the upstream and downstream tubes, the following boundary conditions apply:

1. *Real-tube wall boundary*: ψ = constant, $\partial\psi/\partial z = \partial\psi/\partial r = 0$.

2. *Stream-tube boundary and tube center line*: ψ = constant, $\partial\psi/\partial z = 0$.

3. *End conditions*: For $z = -\infty$, $\partial\psi/\partial z = 0$ and $\psi = f_1(r)$, determined from a uniform velocity for the case of a stream tube or from a fully developed velocity profile for the case of a real tube, for $z = +\infty$, $\partial\psi/\partial z = 0$, and $\psi = f_2(r)$ determined from a fully developed velocity profile. Macrocontinuity is satisfied, $(AU_0)_{-\infty} = (AU_0)_{+\infty}$.

The introduction of the standard central-difference-approximation formulas for the various derivatives in Equations (7) and (8) produces the finite-difference analogs of these equations, which may then be explicitly solved for ψ at each grid point of the solution space. The difference equations were modified for the grid points adjacent to a boundary (5). Equation (8) is used for that portion of the interior of the solution where $\xi \neq 0$; due to the discontinuities of the derivatives of the transformation function, given by Equation (1), the finite-difference form of Equation (7) is used at $\xi = 0$. Point axial and radial velocities are then computed from the point values of the stream function by use of the finite-difference forms of the stream-function-velocity relationships, Equation (6); and the pressure gradient is computed from the finite-difference form of Equation (3) in terms of the point values of the stream function.

Many authors represent the excess tube-entrance pressure loss by the pressure-correction factor

$$C = -\int_{-\infty}^{Z_e}\frac{2}{\rho U_0^2}\frac{\partial P}{\partial z}dz - \frac{64\,Z_e}{N_{Re}} \quad (9)$$

where N_{Re} is the Reynolds number in the downstream tube and the entrance length Z_e is that distance downstream from the small-tube entrance at which the centerline velocity achieves 99% of its fully developed value. Equation (9) applies to the ST-RT case (frictionless upstream tube wall). Analogous relationships define C for the RT-RT case (5).

A disadvantage in the use of C is that it approaches an infinite value as N_{Re} approaches zero. A very sensitive method for characterizing the excess pressure drop in the entrance region employs the pressure-correction ratio

$$C_R = \frac{\text{Actual pressure loss in } Z_e \text{ plus upstream excess pressures}}{\text{Fully developed pressure loss in } Z_e} \quad (10)$$

which is finite for all N_{Re} (*5*). In application, C_R is combined with entrance-length data. However, it is probably more convenient to use L_{eq}, the length of small tube generating, in fully developed flow, a pressure loss equal to the excess pressure loss attributable to the contracted-flow process and to the development of flow in the small-tube entrance region.

FLOW THROUGH A STREAM-TUBE/REAL-TUBE CONTRACTION

This flow model might represent an idealization of flow from a chamber into an array of parallel holes in a flat surface—such as, into the holes of a fiber-spinnerette plate or into the tubes of a shell-and-tube heat exchanger or reactor. For the case in which $\beta = 1$, the model is identical to that used by Vrentas, Duda, and Bargeron (*15*). This case is closely related to the many published analyses of flow in the entrance region of a tube, [for example (*6* to *8*)], with the exception that the axial diffusion of momentum is allowed and a flat velocity profile at the tube entrance is not assumed. Except in the case of special geometries, this latter assumption leads to increasingly larger errors with decreasing Reynolds numbers below N_{Re} of about 200 (*5, 6, 15*).

In our computations for the ST-RT contraction model, the contraction ratio β was varied from 1 to 4; and for most of the computations, N_{Re} was varied from 0.01 to 100, with computations up to 500 for $\beta = 1$. Stability problems arose at N_{Re} greater than about 100, depending on the program, and severely limited the number of computations that could be made. The velocity profiles in Figure 1 show that for $N_{Re} = 1$ and $\beta = 1$ axial diffusion of vorticity causes velocity-profile development to begin more than one-half diameter upstream from the tube entrance. Figure 2 illustrates that for increasing values of N_{Re} momentum overcomes the axial-vorticity transport and that at $N_{Re} \gtrsim 200$ and $\beta = 1$ profile development takes place almost entirely within the tube. Typical radial-component velocity profiles are shown in Figure 3 for $N_{Re} = 50$, $\beta = 1$.

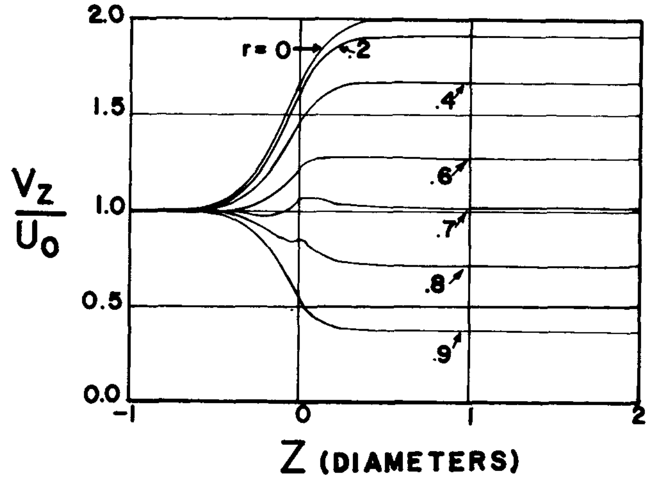

Fig. 1. Axial velocities versus axial position, computed for ST-RT flow, $N_{Re} = 1$, and $\beta = 1.0$ by VT-R method using 20 × 20 grid.

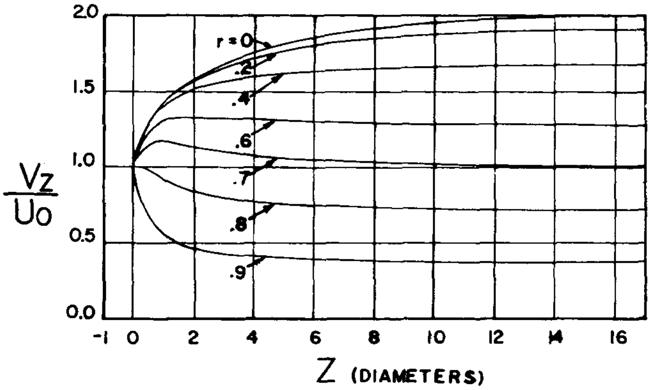

Fig. 2. Axial velocities versus axial position for ST-RT flow, $N_{Re} = 250$, and $\beta = 1.0$, computed by VT-R method using 20 × 20 grid.

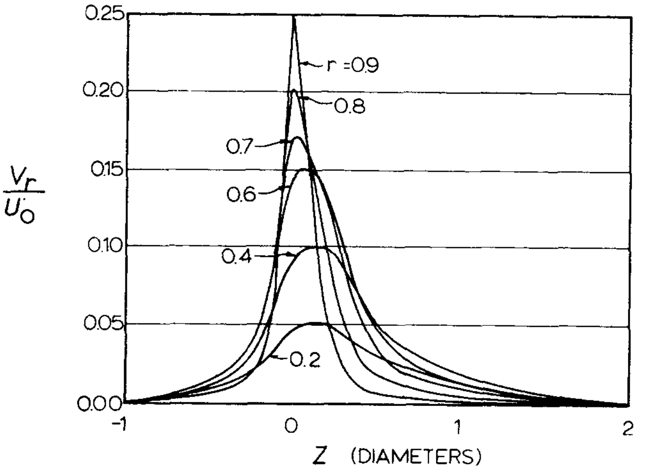

Fig. 3. Radial velocities versus axial position for ST-RT flow, $N_{Re} = 50$, and $\beta = 1.0$ from VT-R method using 20 × 20 grid.

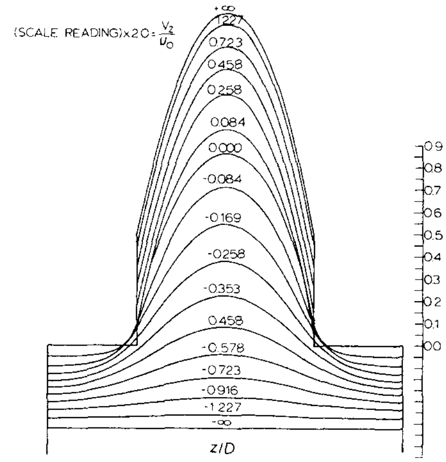

Fig. 4. Axial velocities versus radial and axial position for ST-RT flow, $N_{Re} = 0.01$, and $\beta = 2$ from QL-ML method using 10 × 20 grid. (Zero references for stream tube profiles minus infinity up to minus 0.084 are on scale adjacent to streamtube section).

The values of C, C_R, Z_e, and Z_e/N_{Re} computed using the VT-R program of this investigation (*5*) and $\beta = 1.0$ are compared in Table 1 with those of Vrentas et al. (*15*) for a similar solution, those from boundary-layer solutions of Campbell and Slattery (*4*) and of Collins and Schowalter (*7*), and those from numerical solutions of restricted forms of the equation of motion by Christiansen and Lemmon (*6*), by Vrentas et al. (*15*), and by Hornbeck (*8*). In the latter five solutions, a uniform tube-entrance velocity was assumed. In general, the agreement is satisfactory.

Typical entrance-region velocity profiles, computed using the QL-ML method, are shown in Figures 4 and 5;

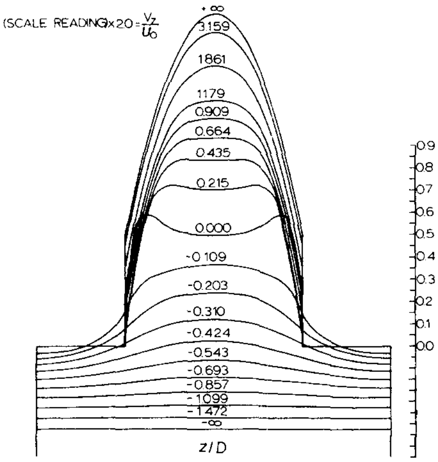

Fig. 5. Axial velocities versus radial and axial position for ST-RT flow, $N_{Re} = 100$, and $\beta = 2$ from QL-ML method using 10 × 20 grid.

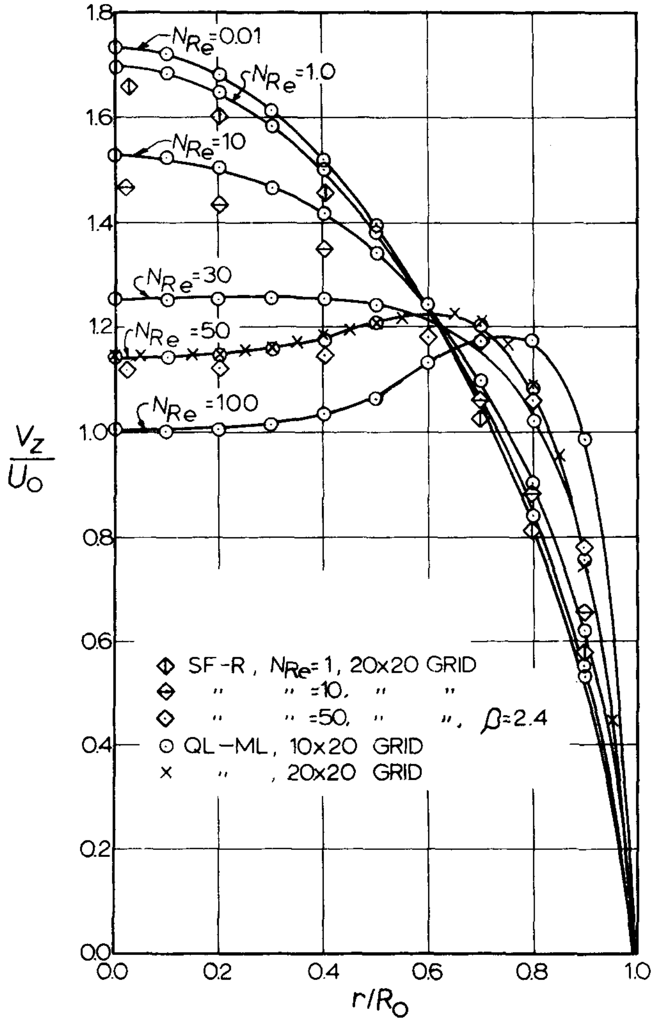

Fig. 6. The dependence of axial velocities at the tube entrance on radial position and N_{Re} for ST-RT flow at $\beta = 2$.

and entrance-velocity profiles are presented in Figures 6 and 7. As indicated in Figures 4 and 5, the velocity profiles begin to deform about 1.2 to 1.5 diameters upstream of the entrance for $\beta = 2$. The effect of axial diffusion extends further upstream of the entrance with greater β.

At N_{Re} between 30 and 50 and larger, a concavity exists in the entrance-velocity profile, as previously reported for flow between parallel plates (16) and in a tube at $\beta = 1$ (*15*). At $\beta = 1$, the concavities are relatively small (a few tenths of a percent). However, the uniform entrance-velocity computations of Atkinson et al. for "creeping" flow in a tube (2) and those of Wang and Longwell (*16*) for flow between parallel plates at $N_{Re} = 300$ indicate concavities an order of magnitude higher. The depth of the concavity increases with β and with N_{Re}.

Of particular interest is the excellent agreement of computations using QL-ML for 10 and 20 radial grid points, shown in Figures 6 and 7 at $N_{Re} = 50$. Axial velocities from the 10-grid computations using SF-R and those from the 20-grid computations using SF-R or VT-R usually agreed to within 1 or 2%. However, some 20 × 20-grid SF-R data are as much as 2 to 5% lower than those from QL-ML computations. As illustrated in Figure 7, the effect of β on entrance-velocity profiles is relatively small for ST-RT flow. The data indicate that contracted-flow entrance velocities are never uniform and that they are only approximately uniform at N_{Re} of about 30 and greater.

Entrance lengths, computed by use of a 20 × 20-grid field and the SF-R method, are compared with data from QL-ML computations in Figure 8. In the case of the RT-RT plots, the lines are drawn through the few 20 × 20-grid data and interpolations from the 10 × 20-grid data, which are about 10% smaller at low N_{Re} and about 5%

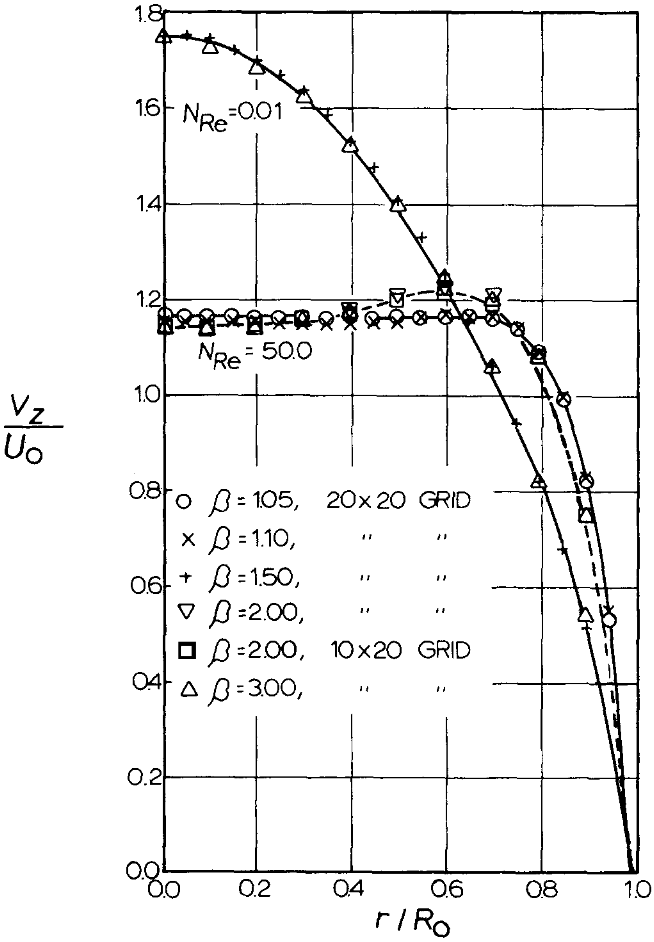

Fig. 7. The dependence of axial velocities at the tube entrance on β for ST-RT contracted flow, computed by QL-ML method.

smaller at $N_{Re} = 200$. It will be noted that for the ST-RT case entrance lengths predicted by extrapolation to $\beta = 1$ of the 20 × 20-grid SF-R data are 2 to 10% longer than those computed from the 20 × 20-grid VT-R program for the same case (see Table 1). The agreement between the SF-R and the QL-ML computations of Z_e is probably as good as could be expected considering that in some cases the required interpolation could not be very accurately accomplished. At $N_{Re} > 200$, Z_e is given satisfactorily by the results from uniform-entrance-velocity-profile computations for $\beta = 1$ (*6*)

$$\frac{L}{D} = 0.055\, N_{Re}$$

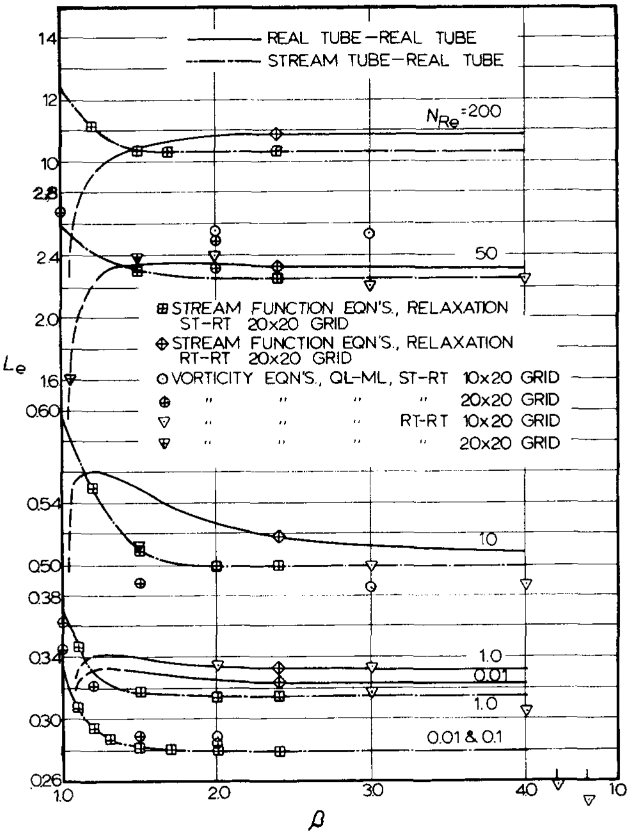

Fig. 8. Tube-entrance lengths Z_e required to achieve 99% of the fully developed center-line velocity for ST-RT and RT-RT contracted flow.

In Figure 9, values of L_{eq} for ST-RT contracted flow are plotted as a function of N_{Re} for $\beta = 1$ to 3. Computations for both 10 × 20 and 20 × 20 grids are included. The results of the similar study by Vrentas, Duda, and Bargeron (*15*) for $\beta = 1$ are shown for comparison, as are the boundary-layer solutions of Collins and Schowalter

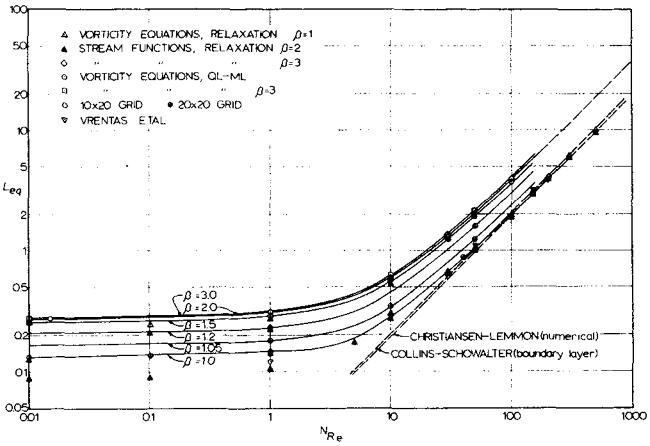

Fig. 9. The dependence of equivalent length on N_{Re} and β for ST-RT contracted flow.

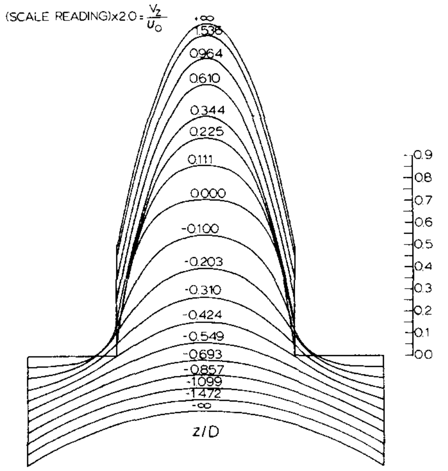

Fig. 10. Axial-velocity profile for RT-RT contracted flow, from QL-ML 10 × 20-grid computation, for $N_{Re} = 10$ and $\beta = 2$.

TABLE 1. COMPARISON OF NUMERICAL COMPUTATIONS FOR $\beta = 1$

	This investigation (*5*)*				Vrentas et al. (*15*)			
N_{Re}	Z_e	Z_e/N_{Re}	C	C_R	Z_e	Z_e/N_{Re}	C	C_R
0.01	0.318	31.8	562.8	1.28				
0.1	0.319	3.19	57.2	1.28				
1.0	0.333	0.333	6.82	1.32	0.33	0.33	7.76	1.37
5.0	0.428	0.086	2.22	1.40				
10.0	0.590	0.059	1.74	1.46				
30.0	1.49	0.050	1.40	1.44				
50.0	2.51	0.050	1.27	1.40	2.35	0.047	1.40	1.47
100.0	5.07	0.051	1.20	1.37				
150.0	8.12	0.050	1.23	1.36	7.19	0.048	1.36	1.44
200.0	11.03	0.055	1.25	1.36				
250.0					13.4	0.054	1.28	1.38
300.0	16.64	0.056	1.28	1.36				
500.0	27.77	0.056	1.23	1.35				

Approximate solutions for conditions at $N_{Re} \gtrsim 200$			
Equations of motion (simplified)	Z_e/N_{Re}	C	C_R
Christiansen and Lemmon (*6*)	0.055**	1.26**	1.36
Hornbeck (*8*)	0.057	1.28	1.35
Vrentas et al. (*15*)	0.056	1.18	1.33
Boundary layer			
Campbell and Slattery (*4*)	0.061	1.18	1.30
Collins and Schowalter (*7*)	0.061	1.33	1.34

* Vorticity-transport equations with relaxation, 20-radial × 20-axial grid.
** Printed as 0.0555 and 1.274 in (*6*).

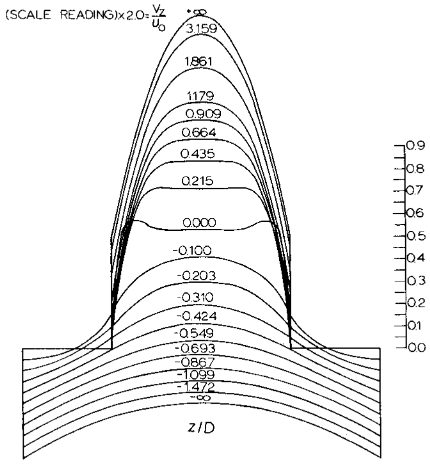

Fig. 11. Axial-velocity profile for RT-RT contracted flow, from QL-ML 10 × 20-grid computation, for N_{Re} = 100 and β = 2.

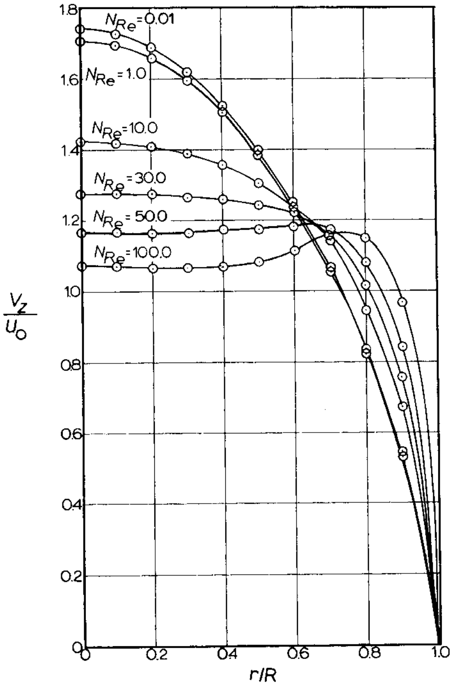

Fig. 12. The dependence of axial velocities at the tube entrance on N_{Re} for RT-RT flow, as determined by 10 × 20-grid QL-ML computations.

(7) and the numerical solutions to restricted forms of the equation of motion by Christiansen and Lemmon (6).

Values of L_{eq} from the three computational methods for β = 1 vary less than about 6% at $N_{Re} \overset{\sim}{>} 30$. Variations in percentages are greater at lower N_{Re} but are less than L_{eq} = 0.1. Three of the four data of Vrentas et al. (*15*) are within the spread of our computed results. It will be noted that the line through the data from the general solutions of the equations of motion for β = 1 become coincident with the line representing the solutions of the restricted equations at N_{Re} = 200 to 250. We are not aware of any experimental data which are sufficiently definitive for evaluation of the ST-RT contracted-flow results.

FLOW THROUGH A REAL-TUBE/REAL-TUBE CONTRACTION

Typical axial-velocity profiles are shown in Figures 10 through 13. The 10 × 20- and 20 × 20-grid QL-ML computations were within 1 or 2% of each other. In the case of the SF-R computations, agreement between 10 × 20- and 20 × 20-grid results was within 1% at r/R < 0.7 and within 2 to 5% at r/R = 0.9 as N_{Re} increased from 0.01 to 50. The SF-R 20 × 20-grid data for β = 2.4, plotted in Figure 13, are consistent with the QL-ML data. Data computed by the QL-ML method are compared in Figure 14 with the experimental data of Burke and Berman (3) determined by a Laser-Doppler procedure for flow of water through a RT-RT contraction β = 4.6. The differences are greater than one would hope, due possibly to round-off error in the computations at this relatively high β and/or to experimental error, which was larger (3) at the relatively low velocities. Burke and Berman observed the concavities at all N_{Re}, which varied from 65 to 340, with maximum velocities up to about 5% greater than the center-line velocities. Uebler (*14*) observed an entrance-velocity concavity of 7.5% at N_{Re} = 75 for flow of a syrup through a contraction. As in the ST-RT geometry, the magnitude of the computed concavity increases with both β and N_{Re} but

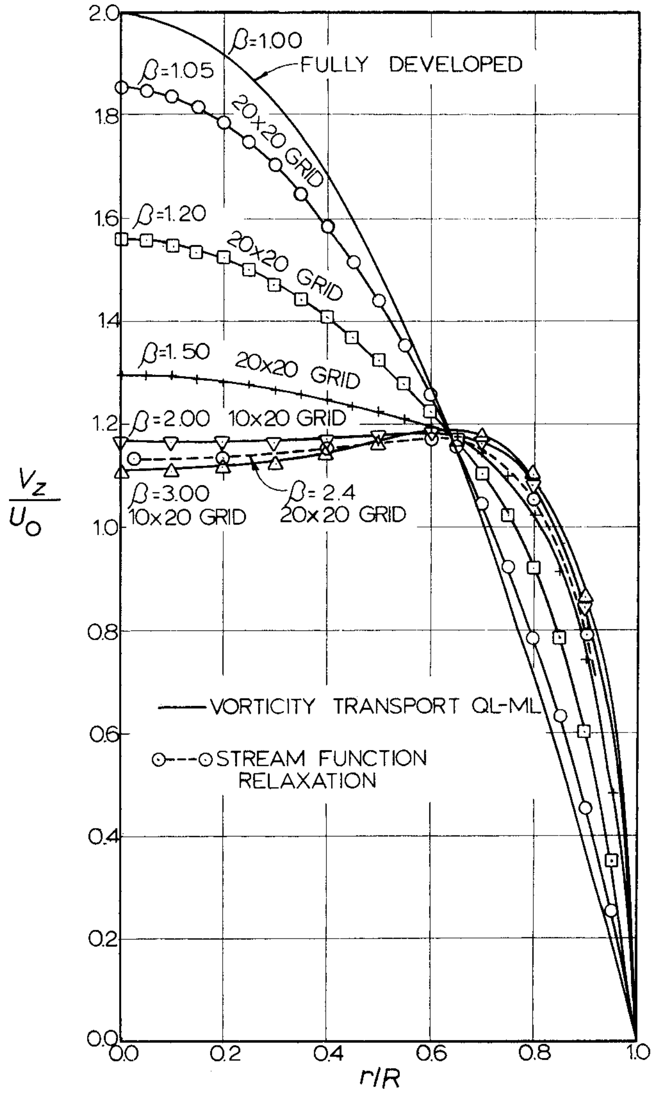

Fig. 13. The dependence of axial velocities at the tube entrance on β at N_{Re} = 50.

is less pronounced in RT-RT contracted flow. Typical radial velocities are shown in Figure 15, while RT-RT entrance-region lengths Z_e are presented in Figure 8 and equivalent lengths L_{eq} are shown in Figure 16. The difference between values of L_{eq} computed by QL-ML and SF-R is, in most cases, less than 5%. The upper-bound excess-entrance-pressure loss determined by Weissenberg (*17*) by means of a variational method for creeping flow from a reservoir of infinite extent into a tube is about 10% higher than our value at $\beta = 8$ and $N_{Re} = 0.01$.

The available experimental excess-pressure-loss data differ greatly with the investigator. Most experimental entrance-pressure-loss data are much larger than computed Newtonian-flow entrance losses, especially at low N_{Re}. The equivalent length L_{eq} increases significantly with the contraction ratio up to a β of about 6 for RT-RT flow, which may account for some of the discrepancies. The data reported by LaNieve and Bogue (*11*) indicate L_{eq} to be about 0.54 for $\beta \simeq 10$ and very low N_{Re} Newtonian flow, which would probably be within the experimental error of our RT-RT computation of 0.31 for $\beta = 8$. However, Astarita and Greco (*1*) and Sylvester and Rosen (*13*) report low N_{Re} values for L_{eq} of 12.4 for $\beta = 2.5$ and of 3 to 5 for $\beta = 8$, respectively, for Newtonian flow. The reasons for these large discrepancies are not clear. However, the discrepancies between our computed data and those of Sylvester and Rosen decrease with increasing N_{Re}; for example, the best line through their glycerine-water data at $N_{Re} > 700$ is less than 3% higher than our RT-RT prediction for $\beta = 6$ (see Figure 16). Also, the average experimental results of LaNieve (*10*) for RT-RT Newtonian flow and $\beta = 11$ for higher N_{Re}, shown in Figure 16, are about 4% lower than our predicted results for RT-RT flow at $\beta = 6$. The only experimental Newtonian datum of LaNieve (*10*) at sufficiently low N_{Re} to be included is also shown and is exactly on his line ($C = 2.53$).

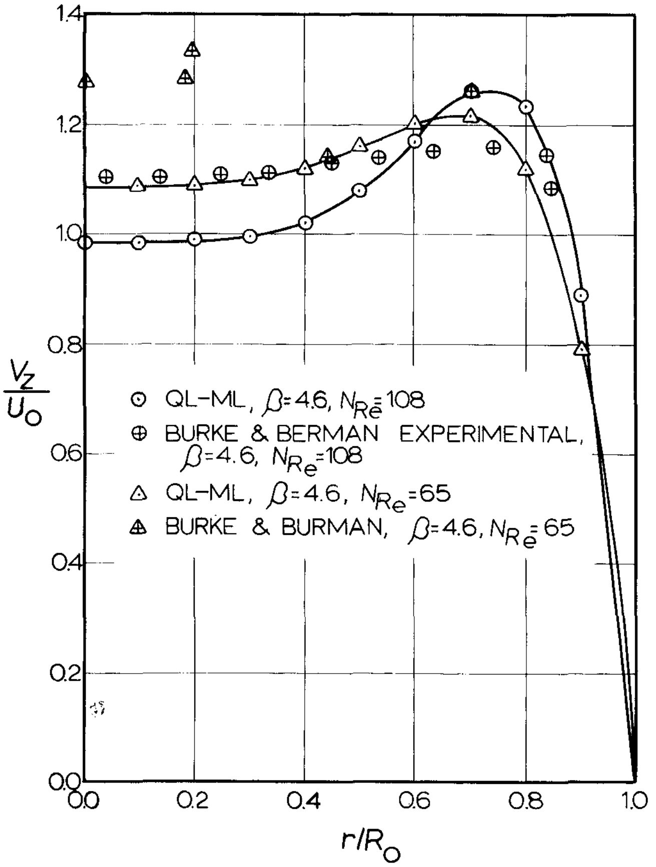

Fig. 14. Comparison of experimentally determined axial velocities with those computed by the QL-ML method using 10 × 20 grid.

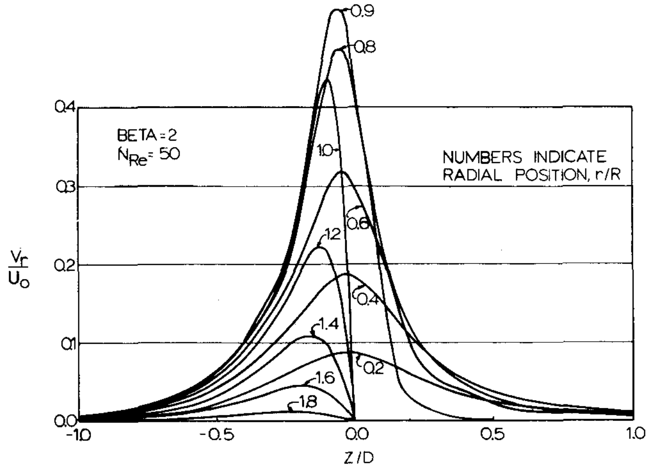

Fig. 15. The dependence of radial velocities on axial position, from QL-ML 10 × 20-grid computations for RT-RT contracted flow at $N_{Re} = 50$ and $\beta = 2$.

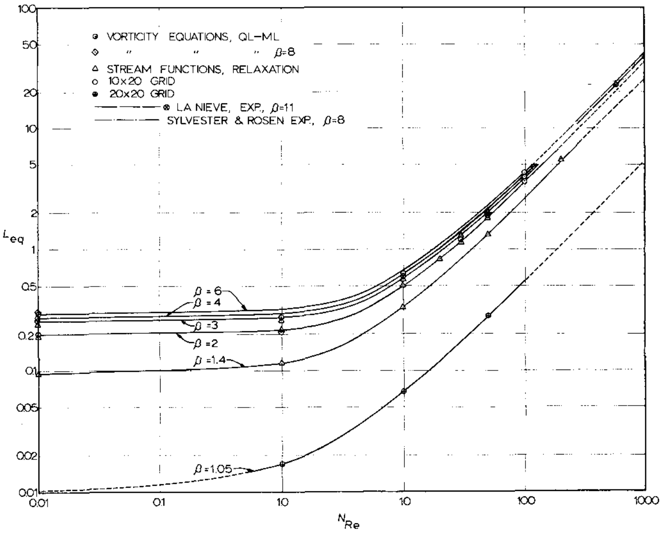

Fig. 16. The dependence of L_{eq} on N_{Re} and β for RT-RT contracted flow.

GENERAL OBSERVATIONS

In both contracted-flow geometries, a stationary vortex just inside the downstream tube (see Figure 17) was computed to exist at N_{Re} of 150 to 200 and greater (*5*, *9*); and a suggestion of a separation was computed at N_{Re} as low as 20 (*9*). The size of this vortex increases with N_{Re} and β. Astarita and Greco (*1*) report experimental pressures (though open to question) which suggest a *vena contracta* for a 41.7% aqueous glycerine solution flowing through a RT-RT contraction at $N_{Re} = 186$ and $\beta = 2.5$ and for water at $N_{Re} = 1346$. The pressure data of LaNieve (*10*) for $\beta = 11$ suggest the presence of a vortex following the tube entrance at $N_{Re} > 400$. He postulated that the lack of evidence for a vortex at $N_{Re} < 400$ might be due to the location of his first small-tube pressure tap too far downstream from the tube entrance. Others (*12*) report experimental velocity profiles for water which do not reveal a *vena contracta* below $N_{Re} = 2100$ for $\beta = 2.0$. Other researchers (*13*) also have reported experimental evidence of a separation. In the RT-RT geometry, a stationary vortex was also computed to exist in the corner formed by the upstream tube and the contraction surface (see Figure 18); the size of this stationary vortex is a function of both β and N_{Re}. For a given value of β and for N_{Re} greater than about 1.0, this vortex diminishes in size with increasing values of N_{Re} and apparently disappears at high N_{Re}; also, for a given value of N_{Re}, it diminishes in size with decreasing values of β. For example, this vortex, though very weak at $\beta < 2$, has been observed experimentally in the flow of aqueous "Methocel" through a contraction, with $\beta = 2.0$ and $N_{Re} = 3.5$ (*12*). We have not detected this torus in the ST-RT case.

In both abruptly contracted flow geometries, the entrance velocity is not uniform. However, the assumption of a uniform entrance velocity becomes a very rough approximation at higher values of N_{Re} and β. For example, at $\beta = 2$, velocity profiles are approximately flat at N_{Re} of 30 to 50 and greater (see Figures 6 and 12).

A necessary but not sufficient condition for high accuracy in such numerical computations as ours is convergence with decreasing size of the grid interval. Both the QL-ML and SF-R computations for 10 × 20- and 20 × 20-grid entrance velocities were usually within about 1% of each other, and values of L_{eq} were usually within 1 to 3% of each other at the higher values of N_{Re}. In the case of SF-R computations 20, 30, and 40 × 20-grid results were essentially the same. Also, QL-ML 10 × 30- and 10 × 40-grid values for L_{eq} were identical and satisfactorily close to 10 × 20-grid results. However, the 10 × 20-grid QL-ML computations appeared closer to convergence than the 10 × 20-grid SF-R computations. In general, a 20 × 20 grid is undoubtedly better; but computational costs would have seriously restricted the range of variables explored. Consequently 10 × 20 grids were used in most of the computations, though in many cases sufficient 20 × 20-grid computations were made to provide a guide for more accurate location of the data plots.

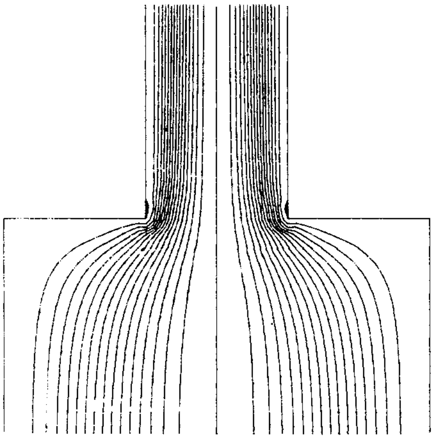

Fig. 17. Interpolated stream functions, computed by the QL-ML method using 10 × 20 grid, for RT-RT contracted flow at $\beta = 3$ and $N_{Re} = 150$.

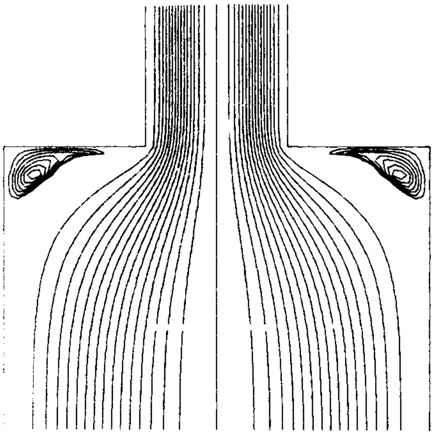

Fig. 18. Interpolated stream functions, computed by the QL-ML method using 10 × 20 grid, for RT-RT contracted flow at $\beta = 3$ and $N_{Re} = 0.01$.

At higher N_{Re}, QL-ML and SF-R values of L_{eq} were usually within 5 to 6% or each other. At low N_{Re}, the QL-ML values of L_{eq} are much larger than the SF-R results—up to almost twice the SF-R results in some cases. However, the absolute difference was always less than $L_{eq} = 0.1$. At low N_{Re}, L_{eq} is obtained from the difference of relatively large numbers; and this may partially account for the discrepancy in the results at low N_{Re}.

Computational instabilities became restrictive beginning in the QL-ML program at N_{Re} of about 100. These instabilities were probably due to a combination of roundoff errors and ill conditioning of the matrix used in determining the initial conditions (9). In the cases of the VT-R and SF-R programs for $\beta = 1$, instabilities became a severe problem at somewhat higher N_{Re}. The SF-R program was felt to be more stable than the VT-R program for $\beta > 1$. However, the QL-ML program converged much more rapidly and yielded equivalent accuracy in much less computer time than did the SF-R program.

CONCLUSIONS

The general equations of motion have been solved numerically for laminar, isothermal, stream-tube/real-tube and real-tube/real-tube contracted flow to yield velocity profiles, entrance lengths, and equivalent lengths that are believed to be sufficiently accurate and convenient for use in the design of equipment and in the analysis of Newtonian-flow data. Additional data are available in (5) and (9).

ACKNOWLEDGMENT

The authors gratefully acknowledge the financial support of the National Science Foundation, the Advanced Research Projects Agency, and the University of Utah Research Fund.

NOTATION

A = area of tube cross section, sq.cm.
A, B, C, D, E, F, G, H = coefficients representing groups of derivatives
C = pressure-correction factor
C_R = pressure-correction ratio
D = diameter of downstream tube, cm.
$f_1(r), f_2(r)$ = functions of radial position
k = constant in Equation (1)
L = length, cm.
L_e = entrance length, diameters
L_{eq} = length of smaller tube in diameters having a developed-flow pressure loss equal to the excess pressure loss attributable to contracted flow and flow development in the entrance region of the small tube
N_{Re} = Reynolds number in general and in downstream tube

P = pressure, dynes/sq.cm.
r = radial distance, cm., or reduced radial distance (r/R)
r/R = reduced radial distance
R_d = radius of smaller or downstream tube, diameters
R_u = radius of larger or upstream tube, diameters
U = z-component velocity, v_z/U_0
U_0 = area average axial velocity in tube (with one or two exceptions, the downstream tube), cm./sec.
v = velocity, cm./sec.
V = r-component velocity, v_r/U_0
z = axial distance, cm., or reduced axial distance (z/D)
z/D = reduced axial distance
Z_e = entrance length, diameters

Greek Letters

β = ratio of large-tube diameter to small-tube diameter
ξ = transformed axial coordinate
ρ = density, g./cu.cm.
ψ = stream function

Subscripts

r = radial direction
z = axial direction

LITERATURE CITED

1. Astarita, G., and G. Greco, *Ind. Eng. Chem. Fundamentals*, 7, 27 (1968).
2. Atkinson, B., M. P. Brocklebank, C. C. H. Card, and J. M. Smith, *AIChE J.*, **15**, 548 (1969).
3. Burke, J. P., and N. S. Berman, Paper 69-WA/FE-13, presented at the ASME Winter Annual Meeting, Los Angeles (November 16-20, 1969).
4. Campbell, W. D., and J. C. Slattery, *Trans. Am. Soc. Mech. Engrs.*, **D85**, 41 (1963).
5. Carter, T. R., Ph.D. thesis, Univ. of Utah, Salt Lake City (1969); also, paper presented at 66th Natl. Am. Inst. Chem. Engrs. Meeting, Portland, Oregon (August, 1969).
6. Christiansen, E. B., and H. E. Lemmon, *AIChE J.*, **11**, 995 (1965).
7. Collins, M., and W. R. Schowalter, *AIChE J.*, **9**, 98 (1963).
8. Hornbeck, R. W., *Appl. Sci. Res.*, **A13**, 224 (1964).
9. Kelsey, S. J., Ph.D. thesis, Univ. of Utah, Salt Lake City (1971).
10. LaNieve, H. L., III, M.S. thesis, Univ. of Tennessee, Knoxville (1963).
11. LaNieve, H. L., III, and D. C. Bogue, *J. Appl. Polym. Sci.*, **12**, 353 (1968).
12. Ramamurthy, A. V., Ph.D. thesis, Monash Univ., Melbourne, Australia (1970); also paper with D. V. Boger, *Trans. Soc. Rheol.*, **15**, 709 (1971).
13. Sylvester, N. D., and S. L. Rosen, *AIChE J.*, **16**, 964 (1970).
14. Uebler, E. A., Ph.D. thesis, Univ. of Delaware, Newark (1966).
15. Vrentas, J. S., J. L. Duda, and K. G. Bargeron, *AIChE J.*, **12**, 837 (1966).
16. Wang, Y. L., and P. A. Longwell, *AIChE J.*, **10**, 323 (1964).
17. Weissenberg, H. L., *J. Phys. of Fluids*, **5**, 1033 (1962).

Manuscript received February 16, 1970; revision received September 20, 1971; paper accepted September 20, 1971.

Stability of Time-Delay Systems

J. G. LANDIS and D. D. PERLMUTTER

School of Chemical Engineering
University of Pennsylvania, Philadelphia, Pennsylvania 19104

A direct method is presented for determining both local and regional stability of systems described by nonlinear differential-difference equations. Prediction of stability is with respect to a general class of initial curves. The practical as well as the conservative nature of the procedure is demonstrated by a numerical example.

The dynamics of many physical systems may be represented by differential-difference equations of the form

$$\frac{d\mathbf{x}}{dt}(t) = \mathbf{f}[\mathbf{x}(t), \mathbf{x}(t-\boldsymbol{\theta})] \tag{1}$$

$$\mathbf{f}[0, 0] = 0$$

where $\mathbf{x}$, $\mathbf{x}(t-\boldsymbol{\theta})$ and $\mathbf{f}$ are vectors of dimension n and the $\boldsymbol{\theta}$ are the values of m time delays. In chemical engineering systems, this form can arise, for example, when the dynamics of the units of a process are represented by differential equations, but the total process includes transport lags between the units. It occurs also when a unit is being controlled via a time-delayed feedback. Such systems can have multiple time delays, nonlinearities, and more than one equilibrium state.

The state of a system described by Equation (1) depends on the value of $\mathbf{x}(t-\boldsymbol{\theta})$, the state variables at some previous times; that is to say, the state will have a continuous dependence on the past history of the system. The solution of Equation (1) is uniquely defined only when initial (past history) curves are specified. In this system initial curves for Equation (1) are analogous to initial conditions in the study of differential equations. Such curves may be defined by

$$\mathbf{x}(t) = \mathbf{x}'(t), \quad (t_0 - \boldsymbol{\theta}) \leqq t \leqq t_0 \tag{2}$$

or equivalently

$$\mathbf{x}(t-\boldsymbol{\theta}) = \mathbf{x}'(t), \quad t_0 \leqq t \leqq (t_0 + \boldsymbol{\theta}) \tag{3}$$

where t_0 represents an initial time, from which equation (1) is to represent the dynamics of the system.

Correspondence concerning this paper should be addressed to D. D. Perlmutter. J. G. Landis is with Air Products and Chemicals Company, Allentown, Pennsylvania.